

Calcium isotope constraints on the end-Permian mass extinction

Jonathan L. Payne^{a,1}, Alexandra V. Turchyn^b, Adina Paytan^c, Donald J. DePaolo^d, Daniel J. Lehrmann^e, Meiyi Yu^f, and Jiayong Wei^g

^aDepartment of Geological and Environmental Sciences, Stanford University, 450 Serra Mall, Building 320, Stanford, CA 94305; ^bDepartment of Earth Sciences, Cambridge University, Downing Street, Cambridge, CB2 3EQ, United Kingdom; ^cInstitute of Marine Sciences, University of California, Santa Cruz, CA 95064; ^dDepartment of Earth and Planetary Science, University of California, 301 McCone Hall, Berkeley, CA 94720-4767; ^eDepartment of Geology, University of Wisconsin, 800 Algoma Boulevard, Oshkosh, WI 54901; ^fCollege of Resource and Environment Engineering, Guizhou University, Caijiaguan, Guiyang 550003, Guizhou Province, China; and ^gGuizhou Geological Survey, Bagongli, Guiyang 550005, Guizhou Province, China

Edited by Andrew H. Knoll, Harvard University, Cambridge, MA, and approved April 1, 2010 (received for review December 4, 2009)

The end-Permian mass extinction horizon is marked by an abrupt shift in style of carbonate sedimentation and a negative excursion in the carbon isotope ($\delta^{13}\text{C}$) composition of carbonate minerals. Several extinction scenarios consistent with these observations have been put forward. Secular variation in the calcium isotope ($\delta^{44/40}\text{Ca}$) composition of marine sediments provides a tool for distinguishing among these possibilities and thereby constraining the causes of mass extinction. Here we report $\delta^{44/40}\text{Ca}$ across the Permian-Triassic boundary from marine limestone in south China. The $\delta^{44/40}\text{Ca}$ exhibits a transient negative excursion of $\sim 0.3\text{‰}$ over a few hundred thousand years or less, which we interpret to reflect a change in the global $\delta^{44/40}\text{Ca}$ composition of seawater. CO_2 -driven ocean acidification best explains the coincidence of the $\delta^{44/40}\text{Ca}$ excursion with negative excursions in the $\delta^{13}\text{C}$ of carbonates and organic matter and the preferential extinction of heavily calcified marine animals. Calcium isotope constraints on carbon cycle calculations suggest that the average $\delta^{13}\text{C}$ of CO_2 released was heavier than -28‰ and more likely near -15‰ ; these values indicate a source containing substantial amounts of mantle- or carbonate-derived carbon. Collectively, the results point toward Siberian Trap volcanism as the trigger of mass extinction.

An abrupt shift in style of carbonate sedimentation occurs across the end-Permian extinction horizon. Microbialites and oolites overlie diverse, fossiliferous limestones of the latest Permian age in carbonate strata deposited across the tropical Tethys (1–8) and in the Panthalassa Ocean (8, 9) (Fig. S1). The mass extinction and facies shift are associated with a large negative excursion in the carbon isotope ($\delta^{13}\text{C}$) composition of carbonate minerals.

Geochemical and sedimentary observations have been used to support various causal mechanisms for the mass extinction. Three different scenarios have been put forth. First, the “Strangelove Ocean” scenario links mass extinction to collapse of the biological pump—the vertical separation in the water column of carbon fixation and respiration, which results from the sinking of organic matter out of the surface ocean (10). Under this scenario, an initial decrease in carbonate deposition would occur because of mixing of surface waters with CaCO_3 -undersaturated deeper waters (assuming an oxygenated deep ocean); subsequent increase in alkalinity because of continental weathering would lead to enhanced carbonate deposition, explaining the deposition of microbialites and oolites (10). Second, the ocean overturn model proposes that extensive sulfate reduction in anoxic deep waters of the Permian oceans resulted in a buildup of carbonate alkalinity and hydrogen sulfide in deep water prior to the extinction event (11–14). Upwelling of these alkaline deep waters would have triggered carbonate precipitation on the shelves (2, 5, 15, 16) and caused mass extinction through combined stresses of hypercapnia, anoxia, and hydrogen sulfide poisoning (14, 15, 17). Third, the ocean acidification model proposes that massive release of ^{13}C -depleted carbon from a reservoir in the crust (e.g., methane clathrates, coal, and magma) (18–22) acidified the ocean, reducing car-

bonate sedimentation and potentially leading to dissolution of carbonate sediments (8). Subsequently enhanced continental weathering and consequent delivery of carbonate alkalinity to the oceans would account for the widespread deposition of microbialites and oolites above the extinction horizon (8).

One avenue for distinguishing among these hypotheses lies in their differing implications for the global cycling of calcium, an element with a residence time of approximately 600–1,000 ky and uniform isotope composition in the modern oceans (23, 24). Isotopes of calcium are fractionated during the precipitation of calcium carbonate (25–27): ^{40}Ca is preferentially incorporated into the solid phase, leaving seawater enriched in ^{44}Ca at steady state relative to the delivery and burial fluxes (24, 28). Consequently, scenarios that require imbalances between the delivery and burial fluxes of calcium in the oceans should impart changes in the calcium isotope composition in the oceans and associated sediments.

We constructed a one-box, isotope mass-balance model of the global calcium cycle (see *Methods* and *SI Discussion*) to generate quantitative predictions for marine calcium isotopes and concentrations associated with the various Permian-Triassic (P/T) boundary scenarios. Fig. 1 illustrates the predictions for these scenarios as well as two alternative possibilities requiring a shift in calcium isotopes only. Both the Strangelove Ocean and acidification scenarios predict an initial decrease in the carbonate depositional flux followed by an increase in carbonate deposition to return the system to steady state, but the perturbation is potentially much larger under the acidification scenario. In contrast, under the ocean overturn scenario one would expect a positive excursion in $\delta^{44/40}\text{Ca}$ because of the stimulation of carbonate precipitation by upwelling of alkaline deep water (2, 5, 15). Oceanographic mechanisms allowing for the overturn scenario have been debated (29–31); here we consider its implications for calcium isotopes irrespective of its feasibility from an oceanographic standpoint. A permanent global shift from calcite- to aragonite-dominated carbonate deposition across the extinction horizon is capable of producing $\delta^{44/40}\text{Ca}$ variation similar to that predicted under the acidification scenario; it causes no change in the calcium concentration of the ocean. A global shift in the isotope composition of the calcium delivery flux within the range of likely values would cause a much smaller and more gradual change in

Author contributions: J.L.P., A.V.T., and A.P. designed research; J.L.P., A.V.T., D.J.D., D.J.L., M.Y., and J.W. performed research; J.L.P., A.V.T., A.P., and D.J.D. analyzed data; and J.L.P., A.V.T., A.P., D.J.D., and D.J.L. wrote the paper.

The authors declare no conflict of interest.

This article is a PNAS Direct Submission.

Freely available online through the PNAS open access option.

¹To whom correspondence should be addressed. E-mail: jlpayne@stanford.edu.

This article contains supporting information online at www.pnas.org/lookup/suppl/doi:10.1073/pnas.0914065107/-DCSupplemental.

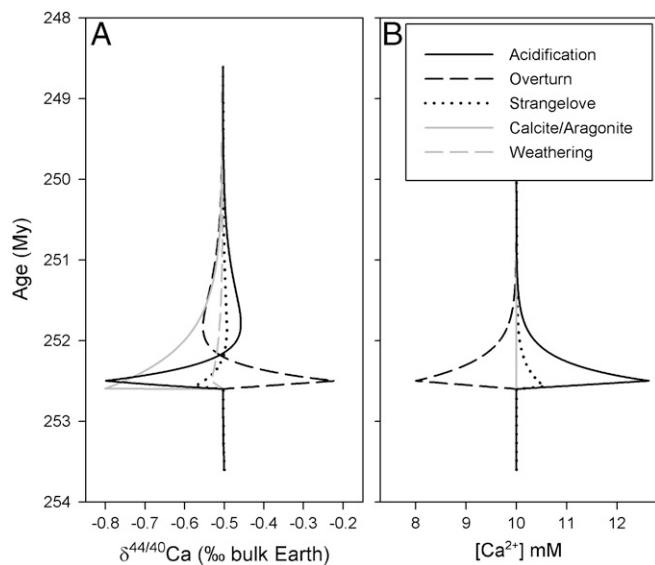


Fig. 1. Output from calcium cycle model under scenarios proposed to explain the P/T boundary $\delta^{13}\text{C}$ excursion and associated deposition of carbonate microbialites and oolites. (A) $\delta^{44/40}\text{Ca}$ in carbonate rocks. (B) Calcium concentration in seawater. The overturn and acidification scenarios are shown under an assumption of a 100-ky perturbation. Also shown are $\delta^{44/40}\text{Ca}$ predictions for a permanent increase by 50% in the proportion of aragonite in carbonate sediment and a 100-ky decrease in the $\delta^{44/40}\text{Ca}$ of the river calcium flux by 0.3%. Modeled calcium concentrations do not change under these last two scenarios. Additional output and sensitivity tests are presented in Fig. S2.

$\delta^{44/40}\text{Ca}$ and no change in the marine calcium concentration (Fig. 1 and Fig. S2).

To constrain changes in global calcium cycling across the P/T transition, we analyzed the $\delta^{44/40}\text{Ca}$ of the micritic fraction of limestone samples from a P/T boundary section at Dajiang, in Guizhou Province, China. P/T boundary strata at Dajiang were deposited above the storm wave base on the Great Bank of Guizhou (GBG), an isolated carbonate platform within the Nanpanjiang Basin (32). The Nanpanjiang Basin is a deep-marine embayment in the Yangtze Block, which was located at approximately 12°N in the eastern Tethys during Early Triassic time (33). The section contains more than 50 m of diverse, fossiliferous packstone and grainstone of the Upper Permian Wujiaping Formation, which contains fusulinid and nonfusulinid foraminifers, calcareous green and red algae, rugose corals, crinoids, brachiopods, calcareous sponges, and gastropods (5, 34). The Wujiaping Formation is overlain by a 15-m-thick thrombolitic microbialite deposited in the immediate aftermath of the mass extinction (*Hindeodus parvus* conodont zone) (35), which contains a low-diversity assemblage of foraminifers, gastropods, and bivalves with rare echinoderms and calcitic and phosphatic brachiopods (4, 5). The microbialite is overlain by 1–2 m of molluscan and brachiopod packstone with rare echinoderms. Above the thin packstone interval are 47 m of thinly bedded, poorly bioturbated micritic limestone. The Lower Triassic section continues with 95 m of dolomite and dolomitized ooid-bearing crystalalgal laminate overlain by 225 m of peritidal limestone cycles (5, 36). Carbonate sediments continued to accumulate on the GBG through Middle Triassic time, reaching a total thickness of nearly 2 km before the platform drowned early in the Late Triassic (32). The GBG was buried in siliciclastic sediments during Late Triassic time, reaching a maximum burial depth of 2.5–3 km (37). Representative P/T boundary facies are illustrated in Fig. S1.

Results

Fig. 2 illustrates the P/T $\delta^{44/40}\text{Ca}$ and $\delta^{13}\text{C}$ records from the Dajiang section, along with age constraints from conodont bio-

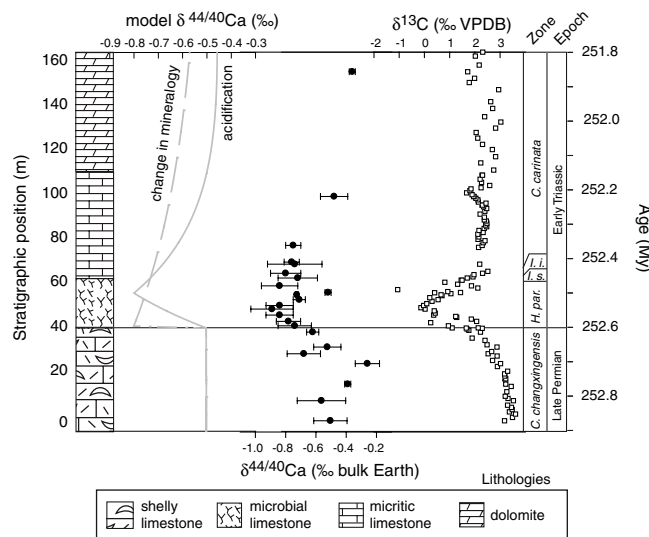


Fig. 2. Lithostratigraphy and calcium and carbon isotope data from the Dajiang section. Error bars indicate one standard deviation between replicate measurements. Carbon isotope data from ref. 65. Conodont zones from refs. 66 and 67. A constant depositional rate of 160 m/My is assumed for the numerical time scale in order to facilitate comparison to model output; the assumed rate is compatible with constraints on the platform (37) and an age of 252.6 My for the extinction horizon (68). Model output for the acidification scenario and the change in mineralogy are shown. See Table S4 for raw data.

stratigraphy and geochronology and model output for the acidification scenario (our preferred scenario; see Discussion below) and a scenario involving a global shift from calcite- to aragonite-dominated carbonate deposition. The $\delta^{44/40}\text{Ca}$ averages approximately -0.6‰ in Permian strata. It decreases by $\sim 0.2\text{‰}$ across the extinction horizon and by $\sim 0.3\text{‰}$ from mean uppermost Permian values to the minimum in the basal Triassic (*H. parvus* zone), 8 m above the extinction horizon (Fig. 2). Although many individual pre- and postexcursion samples exhibit values within error of one another, the average value among samples within the excursion is significantly different from that for the preexcursion samples (Mann–Whitney test; $p = 0.0006$).

Several lines of evidence suggest that the $\delta^{44/40}\text{Ca}$ measurements are primary. The $\delta^{44/40}\text{Ca}$ shift coincides with the globally recognized negative $\delta^{13}\text{C}$ excursion (38), and the $\delta^{44/40}\text{Ca}$ values are significantly correlated with the $\delta^{13}\text{C}$ values (Pearson's $r = 0.62$; $p = 0.002$) but not with indicators of precipitation rate or diagenesis such as Sr/Ca, Mn/Sr, or $\delta^{18}\text{O}$ (Fig. S3). The preexcursion isotope composition (approximately -0.6‰ versus bulk Earth or $+0.6\text{‰}$ versus SRM-915a) is in agreement with Permian values from a Phanerozoic compilation of $\delta^{44/40}\text{Ca}$ values for carbonate rocks and well-preserved shell calcite (39). The light values in $\delta^{44/40}\text{Ca}$ continue from the microbialite facies into overlying micritic limestones before trending back toward preexcursion values (Fig. 2), suggesting that variation in $\delta^{44/40}\text{Ca}$ does not simply reflect differences among facies in either primary fractionation of calcium isotopes or later diagenetic alteration. Finally, similar to the $\delta^{13}\text{C}$ of carbonate rocks, there is far more calcium in the mineral than the pore fluids, helping buffer the $\delta^{44/40}\text{Ca}$ of carbonate minerals against alteration during burial diagenesis (40).

Discussion

The P/T boundary $\delta^{44/40}\text{Ca}$ excursion is inconsistent in direction with the prediction for ocean overturn and is larger in magnitude than the excursion predicted under the Strangelove Ocean or through a change in the isotope composition of weathered calcium. The $\delta^{44/40}\text{Ca}$ excursion is consistent in direction, magnitude, and

time scale with ocean acidification or a large shift in the proportional deposition of aragonite versus calcite. The $\delta^{44/40}\text{Ca}$ excursion could also result from a local (not global) change in isotope fractionation during carbonate precipitation or a change in the local $\delta^{44/40}\text{Ca}$ composition of seawater. Below, we consider the support for these local factors before addressing the global scenarios.

One possibility is that there is a temperature component to the $\delta^{44/40}\text{Ca}$ excursion. Calcium isotope fractionation decreases with increasing temperature (41). Because temperatures increased across the P/T boundary (42), the temperature effect tends in the opposite direction from the observed excursion, reducing its apparent magnitude. The amount of warming across the boundary is poorly constrained, but an increase of 5–10 °C (43, 44) could reduce the fractionation by as much as 0.1–0.2‰ (26, 41). Thus, the negative excursion in seawater $\delta^{44/40}\text{Ca}$ may be somewhat larger than reflected in the raw data.

An alternative mechanism for locally changing the $\delta^{44/40}\text{Ca}$ of carbonate minerals is through a change in the local precipitation rate. Sr/Ca can serve as a proxy for precipitation rate (41); it is not correlated with $\delta^{44/40}\text{Ca}$ in our samples (Fig. S3), suggesting that variation in precipitation rate does not explain the calcium isotope excursion. Moreover, the range of fractionation associated with typical modern carbonate precipitation rates is small (40 and references therein).

The isotope excursion could also reflect a change in the local, and not global, $\delta^{44/40}\text{Ca}$ composition of seawater. There is no evidence for a significant $\delta^{44/40}\text{Ca}$ gradient in the modern oceans (23), but stratigraphic variability in the isotope composition of ancient carbonates has been suggested to result from limited mixing between the open ocean and tectonic basins or epeiric seaways (45). The $\delta^{13}\text{C}$ excursion on the GBG, however, has been observed in carbonate sections across the globe (46, 47) and appears to be representative in terms of relative change in isotope composition as well as in absolute value. Any oceanographic gradient in $\delta^{44/40}\text{Ca}$ would therefore need to have existed in the absence of a similar gradient in $\delta^{13}\text{C}$. Consequently, we view a changing local $\delta^{44/40}\text{Ca}$ gradient as unlikely.

A shift in mineralogy of carbonate sediment from calcite to aragonite could produce a negative excursion in $\delta^{44/40}\text{Ca}$ of carbonate rocks because aragonite is ~0.6‰ lighter than calcite relative to source fluid (26). The observed $\delta^{44/40}\text{Ca}$ excursion of 0.3‰ would thus require that half of the sediment pool in the ocean switched from calcite to aragonite across the extinction horizon. If the shift in mineralogy was only local, then the isotope recovery would require a local return to calcite-dominated sedimentation; if it was global and permanent, then the excursion decays because the global ocean approached a new steady state with a heavier $\delta^{44/40}\text{Ca}$ of seawater because of the globally lighter $\delta^{44/40}\text{Ca}$ in carbonate sediments (Fig. S2). The global scenario is consistent with the greater relative abundance of aragonite-versus calcite-producing skeletal animals globally in the Lower Triassic (48), with petrographic evidence for an originally aragonitic mineralogy for Early Triassic ooids and carbonate crystal fans (5), and with the similarity of Lower Triassic carbonate strata across the global tropics (8).

Finally, the excursion could reflect a decrease in the global $\delta^{44/40}\text{Ca}$ of seawater. Such a decrease is most plausibly generated by ocean acidification (Fig. 1), which would reduce the carbonate ion concentration and carbonate saturation level of seawater and therefore allow calcium to accumulate. The calcium delivery flux is coupled to the dominant burial flux of carbonate sedimentation (F_{carb}) through the carbonate saturation state of seawater:

$$F_{\text{carb}} = k(\Omega - 1)^\eta \quad [1]$$

where k is a scaling constant, η is the order of the reaction [approximately 2 (refs. 10 and 49)], Ω is the saturation state with respect to calcite or aragonite ($\Omega = [\text{Ca}^{2+}][\text{CO}_3^{2-}]/K_{\text{sp}}$), and K_{sp}

is the solubility product of the relevant carbonate mineral (50). Therefore, the effect of elevated calcium delivery via rivers, for example, is mitigated by an increase in Ω , which causes F_{carb} to increase concomitantly. An increase in seawater $[\text{Ca}^{2+}]$ is most likely to result from decreases in k and/or $[\text{CO}_3^{2-}]$. The loss of skeletal carbonate sinks following the end-Permian mass extinction (34) may have caused k to decrease because skeletal animals and algae had been expending metabolic energy to drive carbonate precipitation prior to the extinction. A decrease in $[\text{CO}_3^{2-}]$ and an increase in the calcium river flux are expected under scenarios of CO_2 or methane release previously proposed to account for the negative excursion in $\delta^{13}\text{C}$ (51–53): Because CO_2 is a weak acid (and methane oxidizes to CO_2 within years), rapid CO_2 input would lower ocean pH and $[\text{CO}_3^{2-}]$, reduce Ω and F_{carb} , and thereby allow calcium to accumulate in seawater while simultaneously warming the climate and accelerating the weathering of calcium-bearing rocks. If acidification caused the oceans to become undersaturated with respect to calcite, calcium could also have been released into seawater through dissolution of marine carbonate sediments.

The magnitude of excess calcium delivery required to explain our measured $\delta^{44/40}\text{Ca}$ excursion under this acidification scenario can be calculated by mass balance, assuming a known isotopic composition of the calcium input and the starting size of the marine calcium reservoir. Because the mass extinction event occurred over less than 500 ky and likely less than 150 ky (54), we can approximate the event as instantaneous (see *SI Discussion*, Tables S1 and S2, and Fig. S4). Assuming that the input $\delta^{44/40}\text{Ca}$ is isotopically similar to the river calcium flux and that the ocean $\delta^{44/40}\text{Ca}$ was 1.4‰ heavier than our measured preextinction $\delta^{44/40}\text{Ca}$ (i.e., fractionation similar to modern), we calculate an increase in seawater $[\text{Ca}^{2+}]$ of 21% (2.15 mM) for a 0.2‰ excursion or 36% (3.6 mM) for a 0.3‰ excursion (see *SI Discussion*). Here we have ignored the potential effects of changing temperature and mineralogy in order to investigate the effects of acidification alone. Because expected effects of temperature and mineralogy work in opposing directions (given increases in temperature and prevalence of aragonite) and the likely magnitudes of their effects are similar, in aggregate they may have mostly offset one another.

We favor the ocean acidification scenario over a change in sediment mineralogy as the explanation for the calcium isotope excursion because it also explains a wide range of geochemical, sedimentological, and paleontological observations associated with the P/T boundary not predicted by a shift in carbonate mineralogy alone. First, the synchronous deposition of microbialites and oolites across the global tropics within the *H. parvus* conodont zone (7, 8) could reflect rapid carbonate deposition resulting from enhanced silicate and carbonate weathering in the aftermath of a CO_2 release event. The weathering hypothesis can explain why synchronous, widespread deposition of these facies is confined to the earliest Triassic, despite the persistence of ocean anoxia (55) and skeleton-poor carbonate sediments (34) through much of Early Triassic time. Moreover, removing the calculated $2.2\text{--}3.6 \times 10^{18}$ mol of calcium from the oceans as calcium carbonate would translated to roughly 8–13 m of carbonate sediment on the 10^7 km² of Late Permian carbonate shelves (56), which is broadly consistent with the thickness of the microbialite and oolite deposits within the *H. parvus* zone (Table S3). Second, acidification can explain observations of submarine carbonate dissolution of beds immediately underlying the microbialite (8). Third, rapid CO_2 release can account for the negative excursion in $\delta^{13}\text{C}$ at the P/T boundary (46). Finally, ocean acidification can account for the preferential extinction of heavily calcified marine animals with limited ability to buffer calcifying fluids against changes in ambient water chemistry (17).

If the primary acid added to the oceans was CO_2 , then the $\delta^{44/40}\text{Ca}$ excursion can provide first-order constraints on the magnitude and C-isotope composition of carbon released because

each mole of CO₂ released would allow approximately 1 mol of calcium to be stored in the oceans (57). Assessing the source, magnitude, and isotope composition of carbon released at the P/T boundary has been challenging because the $\delta^{13}\text{C}$ excursion can potentially result from a smaller release from a ^{13}C -depleted source (e.g., biogenic methane) or a larger release from a less depleted reservoir (e.g., coal and basaltic magma). Berner (51) argued that only biogenic methane could account for the magnitude of the $\delta^{13}\text{C}$ excursion, but more recent studies of Siberian Traps intrusions suggest that the magnitude of carbon release may have been larger than previously suspected (22), opening the possibility of carbon release from less depleted reservoirs. One can estimate the $\delta^{13}\text{C}$ of the carbon source as a function of the initial total carbon given the estimated excess calcium delivery ($2.2\text{--}3.6 \times 10^{18}$ mol) and the excursion in $\delta^{13}\text{C}_{\text{carb}}$ (-3.6‰ ; cf. Fig. 2). The likely $\delta^{13}\text{C}$ composition of the CO₂ added on the basis of the above calculation is between -5 and -13‰ (Fig. 3). This calculation assumes that all acidifying power comes from CO₂. However, if emplacement of the Siberian Traps played a significant role (22), then sulfur release could account for as much as half of the acidification [volatile fluxes from flood basalts suggest a molar ratio of CO₂ to SO₂ release of 2.5:1 (58)]. Because H₂SO₄ can acidify the ocean without contributing to the decrease in $\delta^{13}\text{C}$, including its effects in the calculation requires a smaller, and thus isotopically lighter, carbon source. In this more conservative case, only $1.1\text{--}1.8 \times 10^{18}$ mol of CO₂ release would account for the $\delta^{13}\text{C}$ excursion and the $\delta^{13}\text{C}$ of the CO₂ would be between -11 and -28‰ (Fig. 3). Even under this more conservative scenario, the $\delta^{13}\text{C}$ of methane clathrates (-60‰) is far too negative to have been the primary source of carbon; the range of likely values instead points toward a mixture of carbon sources, which appear to have included a substantial component from carbonate rocks and/or mantle-derived volatiles.

Intrusion of Siberian Traps magmas through a thick sequence of carbonate sediments and coal (22) coeval with mass extinction (59) provides a mechanism for releasing sufficient quantities of CO₂ with the appropriate $\delta^{13}\text{C}$ composition through the production of thermogenic methane during the heating of coal (22) and CO₂-rich volatile phases during the incorporation of carbonate rocks into basaltic magma (60). Although previous studies have emphasized the release of carbon from methane clathrates or coal (51–53), $\delta^{44}/^{40}\text{Ca}$ constraints instead suggest that carbon

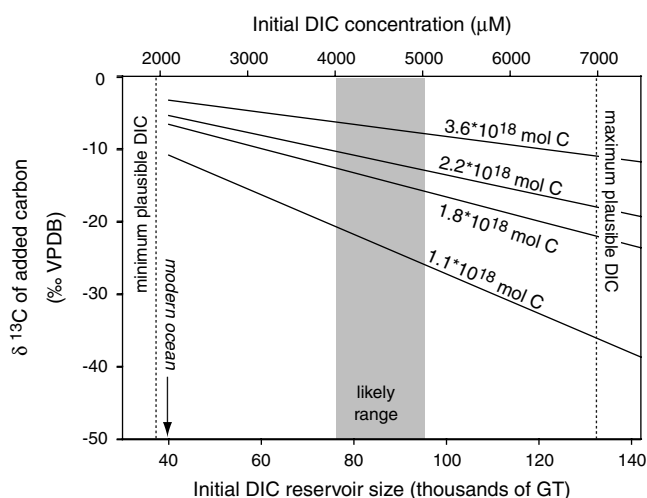


Fig. 3. Carbon isotope composition of carbon added in a P/T boundary perturbation as a function of the initial dissolved inorganic carbon content of the oceans, assuming a $\delta^{13}\text{C}$ excursion from $+3.6$ to 0‰ . Results are shown for calculated upper (3.6×10^{18} mol; 43,200 GT) and lower (1.1×10^{18} mol; 13,200 GT) bounds on the amount of added carbon and intermediate values discussed in the text (1.8×10^{18} mol; 2.2×10^{18} mol).

release associated with the end-Permian extinction may have included a substantial contribution from the incorporation of carbonate country rock into Siberian Traps magmas.

The ocean acidification scenario that we favor for the P/T boundary is similar to that proposed for the Paleocene-Eocene Thermal Maximum (PETM), where there is abundant evidence of a global decrease in the $\delta^{13}\text{C}$ and dissolution of deep-marine carbonate sediments (61) and possibly a negative excursion in $\delta^{44}/^{40}\text{Ca}$ (62). Unlike the end-Permian event, however, the PETM is not associated with global mass extinction—only deep-sea benthic foraminifera were severely affected (63). Differences in the distribution of carbonate sediments between 250 and 55 million years ago may account for much of the contrast. At the PETM, as today, the oceans were buffered against acidification by extensive, fine-grained, unlithified carbonate sediments on the deep-sea floor, which could relatively rapidly dissolve to counter acidification (64). By contrast, the Late Permian deep sea contained no such carbonate buffer because Permian oceans lacked abundant pelagic carbonate producers such as coccolithophorids and planktonic foraminifers. Consequently, any buffering against acidification via dissolution of carbonate sediments could only have occurred more slowly in the less extensive, coarse-grained, mostly lithified, shallow-marine carbonate platform sediments or via chemical weathering of silicate and carbonate rocks on land. Thus, carbonate sediments may not only record critical information constraining the causes of end-Permian mass extinction; their spatial distribution in the oceans may also have been a key control on its severity.

Methods

Notation. Calculation of $\delta^{44}/^{40}\text{Ca}$ follows standard delta notation:

$$\delta^{44}/^{40}\text{Ca} = \left[\frac{^{44}\text{Ca}/^{40}\text{Ca}_{\text{sample}}}{^{44}\text{Ca}/^{40}\text{Ca}_{\text{std}}} - 1 \right] \times 1,000.$$

In this study, $\delta^{44}/^{40}\text{Ca}$ values are referenced to a bulk Earth standard. To compare our numbers to those referenced to the SRM915a scale, our measured value of SRM915a (-1.2‰) can be added to the numbers reported in this work.

Sample Preparation. Samples collected from the outcrop were cut on a rock saw and subsequently ground and polished on a vibrating lapidary tray. The polished face was then drilled with a 1-mm dental bur to produce powder for analysis. Areas of micrite were selected for drilling in samples exhibiting macroscopic variation in carbonate phases. Early and late diagenetic cements, especially fracture-filling vein calcite, were avoided.

Calcium Isotope Analysis. Carbonates were dissolved in SEASTAR acetic acid. Calcium concentrations were determined, and 30- μg Ca aliquots were removed. A 42–48 calcium double spike was added to the aliquots and equilibrated in 5–8 mL of 2N nitric acid. The samples were loaded in 1N nitric acid onto ion separation columns filled with DOWEX® AG 50W-X8 resin. The samples were eluted in 2N nitric acid and dried down. These chemically separated, spiked samples were loaded onto Re filaments with phosphoric acid and measured on a multicollector thermal ionization mass spectrometer. Two replicates of each sample were run, and the standard deviation between replicate measurements is presented.

Trace Metal Analysis. For trace metal analysis, ~ 2 mg of dried, powdered limestone was dissolved in 1M acetic acid. After centrifugation, the supernatant was removed and subjected to trace metal analysis (Mn and Sr) as well as Ca and Mg analysis by using a Thermo Jarrell Ash IRIS Advantage/1000 Radial Inductively Coupled Argon Plasma Spectrometer with a solid state charge induction device detector.

Oxygen Isotope Analysis. For oxygen isotope analysis, samples were reacted with concentrated phosphoric acid at 90 °C in a common acid bath and then measured on a dual inlet mass spectrometer (VG Optima). Isotopic composition is reported in standard delta notation relative to the Vienna Pee Dee belemnite (VPDB) standard. Analytical precision was $\pm 0.1\text{‰}$ (2σ) on the basis of replicate measurements of a laboratory standard.

Geochemical Model. Coupled models of the global calcium and carbon cycles were constructed assuming a one-box ocean and steady-state conditions prior to perturbation.

ACKNOWLEDGMENTS. We thank S. Brown, T. Owens, and A. Jost for assistance with analyses. This study was supported by the Miller Institute for Basic Research and the Canadian Institute for Advanced Research (fellowships to A.V.T.), the Petroleum Research Fund of the American Chemical Society [Grant 45329-G8 (to J.L.P.); Grant 40948 (to D.J.L.)], the National Geographic Society [Grant 8102-06 (to J.L.P.)], the National Science Foundation [CAREER Award (to A.P.); Grant EAR-0807377 (to J.L.P.)], and National Aeronautics and Space Administration [Grant NNX09AN67G (to J.L.P.)].

- Kershaw S, Guo L, Swift A, Fan JS (2002) Microbialites in the Permian-Triassic boundary interval in Central China: Structure, age and distribution. *Facies* 47:83–89.
- Kershaw S, et al. (2007) Earliest Triassic microbialites in the South China block and other areas: Controls on their growth and distribution. *Facies* 53:409–425.
- Kershaw S, Zhang TS, Lan GZ (1999) A microbialite carbonate crust at the Permian-Triassic boundary in South China, and its palaeoenvironmental significance. *Palaeogeogr Palaeoclimatol Palaeoecol* 146:1–18.
- Lehrmann DJ (1999) Early Triassic calcimicrobial mounds and biostromes of the Nanpanjiang basin, south China. *Geology* 27:359–362.
- Lehrmann DJ, et al. (2003) Permian-Triassic boundary sections from shallow-marine carbonate platforms of the Nanpanjiang Basin, south China: Implications for oceanic conditions associated with the end-Permian extinction and its aftermath. *Palaios* 18:138–152.
- Baud A, Cirilli S, Marcoux J (1997) Biotic response to mass extinction: The lowermost Triassic microbialites. *Facies* 36:238–242.
- Baud A, Richoz S, Marcoux J (2005) Calcimicrobial cap rocks from the basal Triassic units: Western Taurus occurrences (SW Turkey). *C R Palevol* 4:569–582.
- Payne JL, et al. (2007) Erosional truncation of uppermost Permian shallow-marine carbonates and implications for Permian-Triassic boundary events. *Geol Soc Am Bull* 119:771–784.
- Sano H, Nakashima K (1997) Lowermost Triassic (Griesbachian) microbial bindstone-cementstone facies, southwest Japan. *Facies* 36:1–24.
- Rampino MR, Caldeira K (2005) Major perturbation of ocean chemistry and a 'Strangelove Ocean' after the end-Permian mass extinction. *Terra Nova* 17:554–559.
- Isozaki Y (1997) Permo-triassic boundary superanoxia and stratified superocean: Records from lost deep sea. *Science* 276:235–238.
- Grice K, et al. (2005) Photic zone euxinia during the Permian-Triassic superanoxic event. *Science* 307:706–709.
- Nielsen JK, Shen Y (2004) Evidence for sulfidic deep water during the Late Permian in the East Greenland Basin. *Geology* 32:1037–1040.
- Kump LR, Pavlov A, Arthur MA (2005) Massive release of hydrogen sulfide to the surface ocean and atmosphere during intervals of oceanic anoxia. *Geology* 33:397–400.
- Knoll AH, Bambach RK, Canfield DE, Grotzinger JP (1996) Comparative Earth history and Late Permian mass extinction. *Science* 273:452–457.
- Grotzinger JP, Knoll AH (1995) Anomalous carbonate precipitates: Is the Precambrian the key to the Permian?. *Palaios* 10:578–596.
- Knoll AH, Bambach RK, Payne JL, Pruss S, Fischer WW (2007) Paleophysiology and end-Permian mass extinction. *Earth Planet Sc Lett* 256:295–313.
- Retallack GJ, Jahren AH (2008) Methane release from igneous intrusion of coal during Late Permian extinction events. *J Geol* 116:1–20.
- Heydari E, Arzani N, Hassanzadeh J (2008) Mantle plume: The invisible serial killer—Application to the Permian-Triassic boundary mass extinction. *Palaeogeogr Palaeoclimatol Palaeoecol* 264:147–162.
- Heydari E, Hassanzadeh J (2003) Deev Jahi Model of the Permian-Triassic boundary mass extinction: A case for gas hydrates as the main cause of biological crisis on Earth. *Sediment Geol* 163:147–163.
- Svensen H, et al. (2004) Release of methane from a volcanic basin as a mechanism for initial Eocene global warming. *Nature* 429:542–545.
- Svensen H, et al. (2009) Siberian gas venting and the end-Permian environmental crisis. *Earth Planet Sc Lett* 277:490–500.
- Zhu P, Macdougall JD (1998) Calcium isotopes in the marine environment and the oceanic calcium cycle. *Geochim Cosmochim Acta* 62:1691–1698.
- Fantle MS, DePaolo DJ (2005) Variations in the marine Ca cycle over the past 20 million years. *Earth Planet Sc Lett* 237:102–117.
- Lemarchand D, Wasserburg GJ, Papanastassiou DA (2004) Rate-controlled calcium isotope fractionation in synthetic calcite. *Geochim Cosmochim Acta* 68:4665–4678.
- Gussone N, et al. (2005) Calcium isotope fractionation in calcite and aragonite. *Geochim Cosmochim Acta* 69:4485–4494.
- DePaolo DJ (2004) Calcium isotopic variations produced by biological, kinetic, radiogenic and nucleosynthetic processes. *Rev Mineral Geochem* 55:255–288.
- De La Rocha CL, DePaolo DJ (2000) Isotopic evidence for variations in the marine calcium cycle over the Cenozoic. *Science* 289:1176–1178.
- Hotinski RM, Bice KL, Kump LR, Najjar RG, Arthur MA (2001) Ocean stagnation and end-Permian anoxia. *Geology* 29:7–10.
- Zhang R, Follows MJ, Grotzinger JP, Marshall J (2001) Could the Late Permian deep ocean have been anoxic?. *Paleoceanography* 16:317–329.
- Meyer KM, Kump LR, Ridgwell A (2008) Biogeochemical controls on photic-zone euxinia during the end-Permian mass extinction. *Geology* 36:747–750.
- Lehrmann DJ, Wei JY, Enos P (1998) Controls on facies architecture of a large Triassic carbonate platform: The Great Bank of Guizhou, Nanpanjiang Basin, South China. *J Sediment Res* 68:311–326.
- Enos P, et al. (2006) *Triassic Evolution of the Yangtze Platform in Guizhou Province, People's Republic of China: Geological Society of America Special Paper 417* (Geological Society of America, Boulder, CO).
- Payne JL, Lehmann DJ, Wei J, Knoll AH (2006) The pattern and timing of biotic recovery from the end-Permian extinction on the Great Bank of Guizhou, Guizhou Province, China. *Palaios* 21:63–85.
- Chen J, Beatty TW, Henderson CM, Rowe H (2009) Conodont biostratigraphy across the Permian-Triassic boundary at the Dawen section, Great Bank of Guizhou, Guizhou Province, South China: Implications for the Late Permian extinction and correlation with Meishan. *J Asian Earth Sci* 36:442–458.
- Lehrmann DJ, Wan Y, Wei JY, Xiao JF (2001) Lower Triassic peritidal cyclic limestone: An example of anachronistic carbonate facies from the Great Bank of Guizhou, Nanpanjiang Basin, Guizhou Province, South China. *Palaeogeogr Palaeoclimatol Palaeoecol* 173:103–123.
- Lehrmann DJ, et al. (2007) Impact of differential tectonic subsidence on isolated carbonate-platform evolution: Triassic of the Nanpanjiang Basin, south China. *AAPG Bull* 91:287–320.
- Corsetti FA, Baud A, Marengo PJRS (2005) Summary of Early Triassic carbon isotope records. *C R Palevol* 4:405–418.
- Farkas J, et al. (2007) Calcium isotope record of Phanerozoic oceans: Implications for chemical evolution of seawater and its causative mechanisms. *Geochim Cosmochim Acta* 71:5117–5134.
- Fantle MS, DePaolo DJ (2007) Ca isotopes in carbonate sediment and pore fluid from ODP site 807A: The Ca²⁺(aq)-calcite equilibrium fractionation factor and calcite recrystallization rates in Pleistocene sediments. *Geochim Cosmochim Acta* 71:2524–2546.
- Tang J, Dietzel M, Böhm F, Köhler SJ, Eisenhauer A (2008) Sr²⁺/Ca²⁺ and ⁴⁴Ca/⁴⁰Ca fractionation during inorganic calcite formation: II. Ca isotopes. *Geochim Cosmochim Acta* 72:3733–3745.
- Korte C, et al. (2004) Carbon, sulfur, oxygen and strontium isotope records, organic geochemistry and biostratigraphy across the Permian/Triassic boundary in Abadeh, Iran. *Int J Earth Sci* 93:565–581.
- Holser WT, et al. (1989) A unique geochemical record at the Permian Triassic boundary. *Nature* 337:39–44.
- Retallack GJ (1999) Postapocalyptic greenhouse paleoclimate revealed by earliest Triassic paleosols in the Sydney Basin, Australia. *Geol Soc Am Bull* 111:52–70.
- Holmden C (2009) Ca isotope study of Ordovician dolomite, limestone, and anhydrite in the Williston Basin: Implications for subsurface dolomitization and local Ca cycling. *Chem Geol* 268:180–188.
- Baud A, Margaritz M, Holser WT (1989) Permian-Triassic of the Tethys—Carbon isotope studies. *Geol Rundsch* 78:649–677.
- Musashi M, Isozaki Y, Koike T, Kreulen R (2001) Stable carbon isotope signature in mid-Panthalassa shallow-water carbonates across the Permo-Triassic boundary: Evidence for C-13-depleted superocean. *Earth Planet Sc Lett* 191:9–20.
- Kiessling W, Aberhan M, Villier L (2008) Phanerozoic trends in skeletal mineralogy driven by mass extinctions. *Nat Geosci* 1:527–530.
- Burton EA, Walter LM (1987) Relative precipitation rates of aragonite and Mg calcite from seawater—Temperature or carbonate ion control?. *Geology* 15:111–114.
- Opdyke BN, Wilkinson BH (1993) Carbonate mineral saturation state and cratonic limestone accumulation. *Am J Sci* 293:217–234.
- Berner RA (2002) Examination of hypotheses for the Permo-Triassic boundary extinction by carbon cycle modeling. *Proc Natl Acad Sci USA* 99:4172–4177.
- Krull ES, Retallack GJ (2000) delta C-13 depth profiles from paleosols across the Permian-Triassic boundary: Evidence for methane release. *Geol Soc Am Bull* 112:1459–1472.
- Erwin DH (1993) *The Great Paleozoic Crisis: Life and Death in the Permian* (Columbia Univ Press, New York).
- Bowring SA, et al. (1998) U/Pb zircon geochronology and tempo of the end-Permian mass extinction. *Science* 280:1039–1045.
- Wignall PB, Twitchett RJ (2002) *Catastrophic Events and Mass Extinctions; Impacts and Beyond: Geological Society of America Special Publication 356*, eds C Koerber and KG MacLeod (Geological Society of America, Boulder, CO), pp 395–413.
- Walker LJ, Wilkinson BH, Ivany LC (2002) Continental drift and Phanerozoic carbonate accumulation in shallow-shelf and deep-marine settings. *J Geol* 110:75–87.
- Caldeira K, Wickett ME (2005) Ocean model predictions of chemistry changes from carbon dioxide emissions to the atmosphere and ocean. *J Geophys Res* 110:C09S04.
- Self S, Thordarson T, Widdowson M (2005) Gas fluxes from flood basalt eruptions. *Elements* 1:283–287.
- Reichow MK, et al. (2009) The timing and extent of the eruption of the Siberian Traps large igneous province: Implications for the end-Permian environmental crisis. *Earth Planet Sc Lett* 277:9–20.
- Iacono Marziano G, Gaillard F, Pichavant M (2008) Limestone assimilation by basaltic magmas: An experimental re-assessment and application to Italian volcanoes. *Contrib Mineral Petr* 155:719–738.
- Zachos JC, et al. (2005) Rapid acidification of the ocean during the Paleocene-Eocene thermal maximum. *Science* 308:1611–1615.
- Griffith EM, Paytan A (2008) *Proceedings of the American Geophysical Union Annual Meeting* (Am Geophysical Union, San Francisco) p B14B-05.
- Thomas E, Shackleton NJ (1996) The Paleocene-Eocene benthic foraminiferal extinction and stable isotope anomalies. *Geol Soc SP* 101:401–441.

64. Archer D, Khesghi H, Maier-Reimer E (1997) Multiple timescales for neutralization of fossil fuel CO₂. *Geophys Res Lett* 24:405–408.
65. Payne JL, et al. (2004) Large perturbations of the carbon cycle during recovery from the end-Permian extinction. *Science* 305:506–509.
66. Ezaki Y, Liu J, Nagano T, Adachi N (2008) Geobiological aspects of the earliest Triassic microbialites along the southern periphery of the Tropical Yangtze Platform: Initiation and cessation of a microbial regime. *Palaios* 23:356–369.
67. Krull ES, et al. (2004) Stable carbon isotope stratigraphy across the Permian-Triassic boundary in shallow marine carbonate platforms, Nanpanjiang Basin, south China. *Palaeogeogr Palaeoclimatol Palaeoecol* 204:297–315.
68. Mundil R, Ludwig KR, Metcalfe I, Renne PR (2004) Age and timing of the Permian mass extinctions: U/Pb dating of closed-system zircons. *Science* 305:1760–1763.

Supporting Information

Payne et al. 10.1073/pnas.0914065107

SI Text

SI Discussion. Ca isotope mass balance—The “instantaneous” calculation. We perform a mass balance calculation to determine how much calcium must be added to the ocean at a specified isotopic composition to decrease the global seawater $\delta^{44/40}\text{Ca}$ by 0.1‰ to 0.3‰. This is done by using a simple mass balance and approximates the event as instantaneous. The mass balance equations used in this calculation are

$$M_f \delta^{44/40}\text{Ca}_f = M_i \delta^{44/40}\text{Ca}_i + M_p \delta^{44/40}\text{Ca}_p \quad [S1]$$

and

$$M_f = M_i + M_p, \quad [2]$$

where M_f is the final mass of calcium, $\delta^{44/40}\text{Ca}_f$ is the final isotope composition of Ca, M_i is the initial mass of Ca, $\delta^{44/40}\text{Ca}_i$ is the initial isotope composition, M_p is the mass of calcium added in the perturbation, and $\delta^{44/40}\text{Ca}_p$ is the isotope composition of the Ca added. Fluid inclusion data suggest that the calcium concentration in the Permian ocean was approximately 10 mM (1). We further estimate $\delta^{44/40}\text{Ca}_i$ of 0.9‰ by assuming that our youngest Permian carbonates are 1.4‰ lighter than coeval seawater values. We assume that calcium added during the perturbation was similar in isotope composition to the river calcium flux and thus estimate $\delta^{44/40}\text{Ca}_p$ of $-0.6‰$.

In the absence of better constraints, we assume that Late Permian delivery and burial fluxes were similar to the modern (2), implying a residence time of Ca in the oceans similar to today, around 1 My (2, 3).

Calcium cycle box model—A time-dependent approach to test the assumptions of the instantaneous calculation. The calcium isotope model was built by following the previous work by DePaolo (2) and Fantle and DePaolo (3). The ocean is treated as a single box with the main fluxes of calcium to the ocean being river input, hydrothermal alteration, and diffusion/dewatering from pore fluid (2, 4), and the main sink is the deposition of carbonate minerals. The equation for the change in calcium concentration with time is

$$\frac{dM_{\text{Ca}}}{dt} = \text{Flux}_{\text{in}} - \text{Flux}_{\text{out}} = F_{\text{riv}} + F_{\text{hyd}} + F_{\text{pw}} - F_{\text{carb}}. \quad [3]$$

The river, hydrothermal, and pore water fluxes are prescribed (F_{riv} , F_{hyd} , and F_{pw} , respectively), and the carbonate sink is prescribed as proportional to the square of the ratio between the current concentration of calcium in the ocean and the steady-state (equilibrium) value (5, 6). Each of these fluxes can be assigned a calcium isotope composition ($\delta^{44/40}\text{Ca}$) such that the changes in calcium concentration and $\delta^{44/40}\text{Ca}$ can be modeled simultaneously. The revised equation is

$$\frac{d(M_{\text{Ca}} \delta_{\text{sw}})}{dt} = F_{\text{riv}} \delta_{\text{riv}} + F_{\text{hyd}} \delta_{\text{hyd}} + F_{\text{pw}} \delta_{\text{pw}} - F_{\text{carb}} (\delta_{\text{sw}} - \epsilon_{\text{carb}}), \quad [4]$$

where δ_{sw} is the $\delta^{44/40}\text{Ca}$ of seawater, δ_{riv} , δ_{hyd} , and δ_{pw} are the $\delta^{44/40}\text{Ca}$ of rivers, hydrothermal input, and pore waters, respectively, and ϵ_{carb} is the fractionation factor between seawater and carbonate minerals. The values used for each of these fluxes in the latest Permian are listed in Table S1.

We solve Eq. 4 above by using finite difference with a time step of 1,000 years and run the model for 5 million years to study the response of the system to prescribed perturbations.

Because the objective here is to probe the response of the calcium cycle to the perturbation at the Permian-Triassic (P/T) boundary, it is less important that the absolute values used are accurate than that they are correct relative to one another. This modeling approach allows us to simulate the system in steady state and examine how the various fluxes respond after a prescribed change.

To examine the predicted consequences for marine calcium concentrations and the $\delta^{44/40}\text{Ca}$ of carbonate sediments under scenarios proposed to account for variation in $\delta^{13}\text{C}$ and carbonate rock facies across the P/T boundary, we ran the model under a variety of perturbation scenarios. These scenarios are described below. Model output for $\delta^{44/40}\text{Ca}$ and $[\text{Ca}^{2+}]$ is presented in Fig. 1. Weathering and burial fluxes of Ca and various sensitivity tests to duration and magnitude of the excursion are presented in Fig. S2.

1. *Strangelove Ocean*: Carbonate sedimentation initially decreases due to collapse of the biological pump and then subsequently increases to slightly exceed steady-state values prior to returning to steady state (7). To simulate this scenario, we reduced carbonate sedimentation by a factor of 24 for 30 ky, the duration of reduced sedimentation under the model of Rampino and Caldeira (7), and then allowed the model to return to its normal dynamics.
2. *Ocean overturn*: Carbonate sedimentation increases due to the mixing of anoxic, alkaline deep waters with oxygenated shallow waters (8). To simulate this scenario, we increased the scaling between calcium concentrations and the carbonate burial flux by a factor 2.06 for 100 ky. The magnitude of forcing was selected such that the marine calcium concentrations decreased by 2 mM over the course of the perturbation. Sensitivity tests were conducted to achieve a similar reduction in $[\text{Ca}^{2+}]$ over different time scales. As discussed in the main text, such a reduction in calcium concentrations corresponds approximately to the amount of calcium stored in microbialite and oolite deposits immediately overlying the end-Permian extinction horizon and thus provides a constraint on the magnitude for this effect.
3. *Ocean acidification*: Carbonate deposition decreases due to ocean acidification and then subsequently increases due to weathering feedbacks. To simulate this scenario, we reduced the carbonate burial flux by 17.7% and increased the calcium weathering flux as much as necessary to produce the magnitude and duration of the desired excursion. We explored durations between 10 and 500 ky for the excursion and magnitudes between 0.1 and 0.3‰. The scenario for a 0.3‰ excursion over 100 ky is presented as the preferred scenario in the main text (Figs. 1 and 2). The results from sensitivity analyses are presented in Fig. S2 and Table S2. Note that this model does not assume any dissolution of existing seafloor carbonate sediments. It merely assumes greatly reduced burial and increased weathering through the river flux. Because the isotope composition of the river flux is similar to that of carbonate sediments (Table S1), we do not explicitly resolve the terrestrial and (possible) marine components of calcium delivery.
4. *Shift from calcite- to aragonite-dominated carbonate deposition*: Calcium isotope composition of sediments (and the ocean) changed due to a change in the ratio of calcite to aragonite production and a consequent global change in the fractionation between seawater and sediments. To simulate this scenario,

io, we assumed an increase of 0.3‰ in the fractionation between seawater and carbonate sediments, as would be predicted if half of the carbonate sediments shifted from calcite to aragonite across the extinction horizon. Under this scenario, seawater calcium concentrations do not change, but seawater $\delta^{44/40}\text{Ca}$ increases while sediment $\delta^{44/40}\text{Ca}$ decreases (temporarily).

5. *Shift in the $\delta^{44/40}\text{Ca}$ composition of the global weathering flux:* Calcium isotope composition of seawater changes due to a change in the isotope composition of the calcium weathering flux. To simulate this scenario, we decreased the $\delta^{44/40}\text{Ca}$ of the river calcium flux by 0.3‰ for time scales of 100 and 500 ky, before returning it to its preexcursion value. We also determined the magnitude of change in the $\delta^{44/40}\text{Ca}$ of the weathering flux to account for a -0.3‰ excursion over 100 and 500 ky. The calculated values (reductions by 3.0 and 0.85‰, respectively) require a global average isotope composition of weathered calcium outside of the range of measured values for igneous and carbonate rocks (2), indicating that the weathering flux cannot plausibly account for the observed isotope excursion.

Calculating excess calcium weathering flux. As discussed in the main text, model–data comparison suggests ocean acidification is the scenario that can best account for the calcium isotope, carbon isotope, sedimentological, and paleobiological observations. The change in the calcium isotope composition of seawater depends primarily on the net imbalance between calcium delivery and burial. Below, we use the calcium isotope model to constrain the magnitude of increase in marine calcium concentrations. Due to uncertainty in time scale and the magnitude of Ca-isotope excursion, we investigate perturbation time scales of 10, 100, and 500 ky by using excursion magnitudes of 0.1‰, 0.2‰, and 0.3‰.

This range of both time scales and excursion magnitudes encompasses the uncertainty in our data and covers many possibilities for the P/T boundary. The smaller magnitude excursion is a conservative estimate of what is observed across the immediate P/T boundary and the latter a realistic estimate of what is observed through the full boundary interval. The shortest time scales represent an end member that may be unrealistic, whereas the longest time scale is, if anything, too long given radiometric constraints. Model results are summarized in Table S2, along with a comparison to results from the instantaneous approximation presented in the main text. Because the box model assumes all excess calcium weathering derives from rivers, we present the results of the instantaneous approximation assuming excess calcium has an isotope composition identical to that of the river flux.

These values provide the excess Ca accumulation in the ocean as a function of excursion magnitude and time scale. The magnitude of excess Ca increases with the time scale of the excursion. As shown in Table S2, results from the time-dependent box model are similar to those derived via the instantaneous approximation described in the main text. The simple model captures the behavior of the system well and the instantaneous approximation is a reasonable one for time scales up to 100 ky.

Carbon isotope mass balance. One benefit of calculating the imbalance between calcium delivery and calcium burial in the oceans is that it puts constraints on the amount of carbon released at this time, assuming ocean acidification was the major cause of calcium accumulation in the oceans. A simple approximation is that each mole of excess calcium requires 1 mol of CO_2 (5). In the case of a more realistic scenario such as volcanism, SO_2 release may accommodate as much as half of the calcium, leaving CO_2 to account for only half of the excess calcium delivery to the oceans (9).

Following an approach analogous to the one described above in relation to $\delta^{44/40}\text{Ca}$, we can perform a simple mass balance calculation to determine how much carbon must be added to the ocean at a specified isotopic composition to decrease the global seawater $\delta^{13}\text{C}$ from $+3.6\text{‰}$ to 0‰ (5). This calculation requires an estimate of the Late Permian dissolved inorganic carbon (DIC) reservoir size. Although there are few direct constraints on this value, Earth system models provide an estimate of the likely range of DIC reservoir sizes. Ridgwell's (10) modeling of Phanerozoic seawater carbonate chemistry suggests a likely DIC concentration of 4,000–5,000 μmol and thus a total reservoir size of $5.5\text{--}6.9 \times 10^{18}$ mol (66,000 to 82,000 GT, where 1 GT = 10^{15} g). The entire range of DIC concentrations over the past 500 My in Ridgwell's model varies between 2,000 (slightly less than modern) and 7,000 μmol (approximately three and a half times modern). These values provide plausible upper and lower bounds. Consistent with Ridgwell's model, previous studies of the P/T $\delta^{13}\text{C}$ record have used estimates between the modern and up to two and a half times the modern for the Late Permian DIC reservoir (8, 11, 12).

The mass balance equations are Eq. 4 from above and

$$M_f \delta^{13}C_f = M_i \delta^{13}C_i + M_p \delta^{13}C_p, \quad [5]$$

where M_f is the final DIC reservoir size, $\delta^{13}C_f$ is the final isotope composition of DIC (0‰) (Fig. 2), M_i is the initial DIC reservoir size, $\delta^{13}C_i$ is the initial isotope composition of the DIC reservoir ($+3.6\text{‰}$) (Fig. 3), M_p is the mass of carbon added in the perturbation, and $\delta^{13}C_p$ is the isotope composition of the carbon added.

Carbon cycle box model—A time-dependent approach to test the assumptions of the instantaneous calculation. The isotope model used for the carbon cycle is a standard one-box model, with a weathering flux of mantle composition (-4.9‰ in these calculations, though the absolute value has little effect within the narrow range of likely values) and separate carbonate and organic carbon burial fluxes. Using Ridgwell's (10) model of Phanerozoic carbonate chemistry in seawater, we assume DIC of 4,500 μM , more than two times modern values. Organic carbon is assumed to be 25‰ lighter than carbonate, with carbonate approximating the bulk seawater average value. We further assume a decrease in the proportion of carbon burial in the organic form (rather than in carbonate minerals) across the P/T boundary (Permian = 0.34, Triassic = 0.275) to be faithful to a change from background values of $\delta^{13}\text{C}$ in the Permian near $+4\text{‰}$ and in the Early Triassic closer to $+2\text{‰}$ (13). Thus, the equilibrium (steady-state) $\delta^{13}\text{C}$ value for the ocean (and carbonate rocks) prior to the excursion is 3.6‰ and postexcursion is $+2\text{‰}$.

We couple the carbon cycle model to the calcium cycle model through the calcium weathering flux from rivers and the calcium burial flux. The excess carbon input (in moles) is assumed to be equal to the imbalance between calcium delivery and calcium burial (5). The burial of carbon in carbonate sediment is assumed to be equivalent to the calcium burial flux. Results are described here and presented in Fig. S4. If all excess calcium is buffered by CO_2 and the excursion is 0.3‰, then the $\delta^{13}\text{C}$ of the CO_2 released must have been close to mantle values. If the excursion was partially buffered by other acids (e.g., SO_2), then the implied $\delta^{13}\text{C}$ of the CO_2 released was more negative. For example, if CO_2 release accounted for only 0.2‰ of the calcium isotope excursion, then its $\delta^{13}\text{C}$ would have been near -14‰ , and if CO_2 release accounted for only 0.1‰ of the calcium isotope excursion, then its $\delta^{13}\text{C}$ would have been near -25‰ . Thus, model calculations indicate that the $\delta^{13}\text{C}$ of carbon released only approaches organic carbon values if the calcium isotope excursion was very small or if carbon only accounted for a small fraction of the acidification event. The nonmonotonic behavior of $\delta^{13}\text{C}$ as a function of excursion time scale in Fig. S4 results from the change in equilibrium $\delta^{13}\text{C}$ incorporated into the model across

the P/T boundary and the response time of C to this shift. More realistic coupling of the calcium and carbon cycles is desirable but would require explicit calculations of not only dissolved inorganic carbon concentrations but also alkalinity and silicate weathering. Given the existing uncertainties in the magnitude of the $\delta^{44}/^{40}\text{Ca}$ excursion and the amount of the excursion accounted for through CO_2 -driven acidification, such additional specificity is not justified by existing data and is beyond the scope of the current study.

In summary, if carbon release buffered the increased calcium concentration in seawater, then that carbon likely had an isotope composition between mantle values and those of organic carbon. However, only under the scenarios involving the least amount of carbon and the shortest time scales do implied $\delta^{13}\text{C}$ values approach those of organic matter (near -25‰). Thus, our results indicate a substantial contribution of carbon heavier in $\delta^{13}\text{C}$ than organic carbon or methane sources. Such carbon was likely derived from the mantle or carbonate rocks.

- Horita J, Zimmermann H, Holland HD (2002) Chemical evolution of seawater during the Phanerozoic: Implications from the record of marine evaporites. *Geochim Cosmochim Acta* 66:3733–3756.
- DePaolo DJ (2004) Calcium isotopic variations produced by biological, kinetic, radiogenic and nucleosynthetic processes. *Rev Mineral Geochem* 55:255–288.
- Fantle MS, DePaolo DJ (2005) Variations in the marine Ca cycle over the past 20 million years. *Earth Planet Sc Lett* 237:102–117.
- Berner EK, Berner RA (1996) *Global Environment: Water, Air, and Geochemical Cycles* (Prentice Hall, Englewood Cliffs, NJ).
- Caldeira K, Wickett ME (2005) Ocean model predictions of chemistry changes from carbon dioxide emissions to the atmosphere and ocean. *J Geophys Res* 110:C09504.
- Opdyke BN, Wilkinson BH (1993) Carbonate mineral saturation state and cratonic limestone accumulation. *Am J Sci* 293:217–234.
- Rampino MR, Caldeira K (2005) Major perturbation of ocean chemistry and a 'Strangelove Ocean' after the end-Permian mass extinction. *Terra Nova* 17:554–559.
- Knoll AH, Bambach RK, Canfield DE, Grotzinger JP (1996) Comparative Earth history and Late Permian mass extinction. *Science* 273:452–457.
- Self S, Thordarson T, Widdowson M (2005) Gas fluxes from flood basalt eruptions. *Elements* 1:283–287.
- Ridgwell AJ (2005) A mid-Mesozoic revolution in the regulation of ocean chemistry. *Mar Geol* 217:339–357.
- Payne JL, Kump LR (2007) Evidence for recurrent Early Triassic massive volcanism from quantitative interpretation of carbon isotope fluctuations. *Earth Planet Sc Lett* 256:264–277.
- Berner RA (2002) Examination of hypotheses for the Permo-Triassic boundary extinction by carbon cycle modeling. *Proc Natl Acad Sci USA* 99:4172–4177.
- Payne JL, et al. (2004) Large perturbations of the carbon cycle during recovery from the end-Permian extinction. *Science* 305:506–509.
- Pilson MEQ (1998) *An Introduction to the Chemistry of the Sea* (Prentice Hall, Upper Saddle River, NJ).
- Elderfield H, Schultz A (1996) Mid-ocean ridge hydrothermal fluxes and the chemical composition of the ocean. *Ann Rev Earth Planet Sci* 24:191–224.
- Amini M, et al. (2008) Calcium isotope ($\delta^{44}/^{40}\text{Ca}$) fractionation along hydrothermal pathways, Logatchev field (Mid-Atlantic Ridge, 14°45'N). *Geochim Cosmochim Acta* 72:4107–4122.
- Fantle MS, DePaolo DJ (2007) Ca isotopes in carbonate sediment and pore fluid from ODP Site 807A: The Ca^{2+} (aq)-calcite equilibrium fractionation factor and calcite recrystallization rates in Pleistocene sediments. *Geochim Cosmochim Acta* 71:2524–2546.
- Sano H, Nakashima K (1997) Lowermost Triassic (Griesbachian) microbial bindstone-cementstone facies, southwest Japan. *Facies* 36:1–24.
- Lehrmann DJ (1999) Early Triassic calcimicrobial mounds and biostromes of the Nanpanjiang basin, south China. *Geology* 27:359–362.
- Lehrmann DJ, et al. (2003) Permian-Triassic boundary sections from shallow-marine carbonate platforms of the Nanpanjiang Basin, south China: Implications for oceanic conditions associated with the end-Permian extinction and its aftermath. *Palaios* 18:138–152.
- Ezaki Y, Liu J, Nagano T, Adachi N (2008) Geobiological aspects of the earliest Triassic microbialites along the southern periphery of the Tropical Yangtze Platform: Initiation and cessation of a microbial regime. *Palaios* 23:356–369.
- Adachi N, Ezaki Y, Liu JB (2004) The fabrics and origins of peloids immediately after the end-Permian extinction, Guizhou Province, South China. *Sed Geol* 164:161–178.
- Galfetti T, et al. (2008) Evolution of Early Triassic outer platform paleoenvironments in the Nanpanjiang Basin (South China) and their significance for the biotic recovery. *Sed Geol* 204:36–60.
- Algeo TJ, Ellwood BB, Nguyen TKT, Rowe H, Maynard JB (2007) The Permian-Triassic boundary at Nhi Tao, Vietnam: Evidence for recurrent influx of sulfidic watermasses to a shallow-marine carbonate platform. *Palaeogeogr Palaoclimatol Palaeoecol* 252:304–327.
- Kershaw S, Guo L, Swift A, Fan JS (2002) Microbialites in the Permian-Triassic boundary interval in Central China: Structure, age and distribution. *Facies* 47:83–89.
- Kershaw S, et al. (2007) Earliest Triassic microbialites in the South China block and other areas: Controls on their growth and distribution. *Facies* 53:409–425.
- Kershaw S., Zhang TS, Lan GZ (1999) A microbialite carbonate crust at the Permian-Triassic boundary in South China, and its palaeoenvironmental significance. *Palaeogeogr Palaoclimatol Palaeoecol* 146:1–18.
- Ezaki Y, Liu JB, Adachi N (2003) Earliest Triassic microbialite micro- to megastructures in the Huaying area of Sichuan Province, South China: Implications for the nature of oceanic conditions after the end-Permian extinction. *Palaios* 18:388–402.
- Heydari E, Hassanzadeh J, Wade WJ, Ghazi AM (2003) Permian-Triassic boundary interval in the Abadeh section of Iran with implications for mass extinction: Part 1-Sedimentology. *Palaeogeogr Palaoclimatol Palaeoecol* 193:405–423.
- Ehrenberg SN, Svana TA, Swart PK (2008) Uranium depletion across the Permian-Triassic boundary in Middle East carbonates: Signature of oceanic anoxia. *AAPG Bull* 92:691–707.
- Baud A, Cirilli S, Marcoux J (1997) Biotic response to mass extinction: The lowermost Triassic microbialites. *Facies* 36:238–242.
- Baud A, Richoz S, Marcoux J (2005) Calcimicrobial cap rocks from the basal Triassic units: Western Taurus occurrences (SW Turkey). *C R Palevol* 4:569–582.
- Baud A, Magaritz M, Holser WT (1989) Permian-Triassic of the Tethys—Carbon isotope studies. *Geol Rundsch* 78:649–677.
- Hips K, Haas J (2006) Calcimicrobial stromatolites at the Permian-Triassic boundary in a western Tethyan section, Bukk Mountains, Hungary. *Sed Geol* 185:239–253.
- Magaritz M, Holser WT (1991) The Permian-Triassic of the Gartnerkofel-1 core (Carnic Alps, Austria): Carbon and oxygen isotope variation. *Abhandlung Geolog Bund* 45:149–163.
- Magaritz M, Bar R, Baud A, Holser WT (1988) The carbon-isotope shift at the Permian Triassic boundary in the Southern Alps is gradual. *Nature* 331:337–339.

Table S4. Calcium isotope compositions of analyzed samples illustrated in Fig. 1

Sample	Stratigraphic elevation (m)	$\delta^{44/40}\text{Ca}$	Standard deviation	$\delta^{13}\text{C}$ (VPDB)	$\delta^{18}\text{O}$ (VPDB)	Sr/Ca	Mn/Sr
PDJ-001	0	-0.50	0.11	3.18	-3.77	0.001781	0.112452
PDJ-009	9	-0.56	0.16	3.53	-2.68	0.001345	0.118056
PDJ-017	17	-0.39	0.02	3.23	-4.78	0.001278	0.17529
PDJ-026	26	-0.26	0.08	3.02	-4.05	0.001085	0.186127
PDJ-030	30	-0.68	0.11	2.52	-5.15	0.001156	0.312711
PDJ-033	33	-0.52	0.09	2.88	-3.44	0.001262	0.333708
PDJ-040	39.7	-0.62	0.04	2.22	-5.31	0.002186	0.109726
PDJ-044	43	-0.74	0.11	0.95	-4.01	0.001261	0.614865
PDJ-046	44.5	-0.78	0.08	2.07	-2.70	0.001243	0.579677
PDJ-050	47	-0.84	0.10	0.37	-4.48	0.001383	0.425197
PDJ-053	50	-0.89	0.14	0.03	-4.22	0.001280	2.563522
PDJ-055	51.6	-0.84	0.09	-0.03	-6.00	0.001288	2.014563
PDJ-058	54	-0.71	0.04	0.54	-3.94	0.001546	0.725183
PDJ-061	56.4	-0.73	0.01	0.66	-4.04	0.001705	0.095718
PDJ-064	57.4	-0.52	0.02	1.43	-4.71	0.001956	0.196133
PDJ-068	60	-0.84	0.12	1.87	-5.32	0.002685	0.034841
PDJ-072	64	-0.72	0.13	1.70	-4.40	0.004116	0.008886
PDJ-075	66	-0.80	0.10	2.31	-4.47	0.001596	0.020517
PDJ-080	70.1	-0.74	0.18	2.19	-4.92	0.003823	0.075784
PDJ-081	71	-0.76	0.05	No data	No data	0.000860	0.251981
PDJ-090	80	-0.75	0.05	2.29	-4.40	0.000768	0.343173
PDJ-100	87.6	-0.85	0.13	2.43	-2.82	0.001781	0.112452
PDJ-115	100.4	-0.48	0.09	1.96	-6.08	0.001345	0.118056
PDJ-140	156.2	-0.36	0.02	1.71	-4.43	0.000700	0.355482